



Bi₂O₃ quantum dots decorated anatase TiO₂ nanocrystals with exposed {001} facets on graphene sheets for enhanced visible-light photocatalytic performance

Jungang Hou, Chao Yang, Zheng Wang, Shuqiang Jiao*, Hongmin Zhu

School of Metallurgical and Ecological Engineering, University of Science and Technology Beijing, Beijing, 100083, China

ARTICLE INFO

Article history:

Received 2 July 2012

Received in revised form 24 August 2012

Accepted 9 September 2012

Available online 16 September 2012

Keywords:

Bi₂O₃ quantum dots

TiO₂ nanosheets

Graphene

Visible light photocatalyst

Degradation

ABSTRACT

Due to its great importance in fundamental research and practical applications, tailored synthesis of anatase TiO₂ dominated with highly energetic {001} facets has attracted extensive interest. Here, Bi₂O₃ quantum dots decorated anatase TiO₂ with exposed {001} high energy facets had been firstly prepared on graphene sheets by a simple and feasible strategy using the hydrofluoric acid. During the synthesis process, TiO₂ nanosheets were homogeneously decorated with surface enrichment of Bi₂O₃ quantum dots and graphene was uniformly covered with a large number of Bi₂O₃/TiO₂ composites. The morphologies, structural properties and photocatalytic performance of the resultant Bi₂O₃/TiO₂/graphene composites were investigated and were characterized by X-ray diffraction, scanning electron microscopy, transmission electron microscopy, X-ray photoelectron spectra, UV–vis diffuse reflectance spectrum and photoluminescence spectra. A certain amount of Bi₂O₃ quantum dots coating on TiO₂ nanosheets exhibited significant improvement in photocatalytic degradation of the azo dye Rhodamine B under visible-light irradiation than TiO₂ nanosheets, which could be attributed to the extending spectral response from UV to visible area, the enhanced photosensitizing effect of the surface enriched Bi₂O₃ quantum dots and the strong interaction between Bi₂O₃ and TiO₂. Furthermore, the Bi₂O₃/TiO₂/graphene hybrids could be used as a stable photocatalyst for the highest photocatalytic activity for Rhodamine B degradation, which is ascribed predominantly to the efficient reduction of electron–hole pair recombination in the heterostructures. This investigation likely opens up new possibilities for the development of highly efficient TiO₂ based photocatalysts that utilize visible-light as an energy source.

© 2012 Elsevier B.V. All rights reserved.

1. Introduction

Environmental pollution and the energy crisis have become two major problems for human society and seriously threaten the existence of terrestrial lives. Photocatalysts have consistently drawn much attention for many of the environmental challenges facing the modern world since it can provide a simple way to use light to perform chemical transformation. In particular, as one of the most important wide-band-gap semiconductors possessing unique chemical, electronic, and optical properties, anatase titanium dioxide (TiO₂) has been studied extensively because of its great potential applications in photovoltaic cells, photo/electrochromics, photocatalysis, photonic crystals, smart surface coatings, and sensors [1–10]. Thus, enormous efforts have been devoted to improving the photocatalytic activity of TiO₂. As the surface structure of photocatalysts play an important role to their photocatalytic activities because the photoelectron conversion takes place only when photoinduced electrons and holes are

available on the surface [11–14]. For anatase TiO₂, theoretical calculations indicate that the {101} facets are the thermodynamically most stable, while the {001} facets are the most reactive facets with a high surface energy [13]. Anatase TiO₂ single crystals mainly exist with a morphology of octahedral bipyramid, in which the majority of the surface is normally enclosed by energetically favorable {101} facets rather than the more reactive {001} facets under equilibrium conditions [15–17]. Thus, it has been a great challenge to synthesize anatase TiO₂ with exposed {001} facets.

Furthermore, to make them visible-light responsive, various titanium sources such as TiN, TiS₂, TiC have been used to prepare nonmetal doped (e.g. N, S, C-doped) anatase TiO₂ with dominating {001} facets [18–21]. Nevertheless, the rapid h⁺/e[−] recombination rate of TiO₂ (an intrinsic drawback) is not essentially improved. It is therefore highly desirable to develop a new modification and/or preparation method that can enhance the photocatalytic activity of TiO₂.

To tackle these drawbacks over TiO₂, different hybrid semiconductor heterostructures have been explored. The aim has been to extend the response range to wider wavelength and to promote greater separation of the photoinduced charge carriers. For example, three-dimensional flower-like hierarchical Bi₂O₃/TiO₂

* Corresponding author. Tel.: +86 10 62334775.

E-mail address: sjiao@ustb.edu.cn (S. Jiao).

architectures synthesized by a simple and direct solvothermal route without any linker shell, showed much higher photocatalytic activity [22]. CdS/TiO₂ heterostructures exhibited superior hydrogen evolution rate from splitting water when compared with either CdS or TiO₂ alone [23]. Bi₁₂TiO₂₀/TiO₂ heterostructures exhibited much higher photocatalytic activity [24]. In this work, we have considered the use of Bi₂O₃ quantum dots to enhance the photoactivity of TiO₂ nanosheets with exposed {001} facets, which has not been reported before to our knowledge.

Since 2004, the fascinating material, graphene, has offered exciting new opportunities in various fields of nanotechnology including photocatalysis based on properties such as large surface area, good flexibility, high electrical conductivity, high chemical stability and tunable surface functional groups [25,26]. Zhang et al. reported graphene–P25 TiO₂ composites synthesized via a facile hydrothermal reaction that exhibited an enhanced photocatalytic activity for the degradation of methylene blue in aqueous solutions [27]. Anatase TiO₂ nanocrystals with exposed {001} facets on graphene sheets via molecular grafting has shown an enhanced photocatalytic activity [28]. Thus, there appears to be great untapped potential for exploring the possibility of using graphene and its oxide to help improve photocatalytic activity with Bi₂O₃/TiO₂/graphene composites.

Herein, we have looked at using two strategies in synergy to improve photocatalytic performance of TiO₂ nanosheets. Firstly, a homogeneous Bi₂O₃ quantum dots decorated TiO₂ nanosheets composites, has been synthesized via a one-pot solvothermal reaction. A certain amount of Bi₂O₃ quantum dots coating on TiO₂ nanosheets exhibited significant improvement in photocatalytic degradation of the azo dye Rhodamine B under visible-light irradiation than TiO₂ nanosheets. Secondly, Bi₂O₃/TiO₂ composites coupled with graphene sheets were prepared by a facile hydrothermal process. An efficient improvement has been found for the same reaction using Bi₂O₃/TiO₂/graphene composites. In the discussion section, a plausible mechanism for photocatalytic reaction in the Bi₂O₃/TiO₂/graphene systems is proposed.

2. Experimental

2.1. Synthesis of Bi₂O₃/TiO₂ nanocomposites

All chemicals were of analytical and were directly used without any treatment. In this work, in a typical procedure, 2.645 mmol Ti(OC₃H₇)₄ and Bi(NO₃)₃·5H₂O, with various molar ratio of Bi: Ti, were dissolved in 0.4 mL HF under vigorous stirring. The reaction solution was transferred into a 50-mL Teflon-lined stainless steel autoclave and kept in an electric oven at 180 °C for 24 h. The autoclave was then taken out of the oven and left to cool naturally to room temperature. To further confirm the enhanced effect of surface fluorination on the photoactivity, the fluorinated surface of TiO₂ nanosheets was cleaned with diluted 0.1 M NaOH solution, resulting in the formation of F-free TiO₂ nanosheets. Besides, the samples with different molar ratios of Bi₂O₃ to TiO₂ (0, 1, 3 and 5 mol%) were labeled as T0, T1, T3 and T5, respectively.

2.2. Synthesis of Bi₂O₃/TiO₂/graphene nanocomposites

Graphite oxide was prepared using the Hummers' method [29], by reacting commercially obtained graphene in a mixture of strong oxidizing agents namely H₂SO₄, NaNO₃ and KMnO₄. The reacted graphene was filtered and washed twice with 1 M HCl and then twice with distilled water. The graphene was then dried forming a brown powder. Varying amounts of graphene were ultrasonicated in 12 mL of deionized water and 12 mL of anhydrous ethanol solution to disperse it well; after that, 0.2 g of the Bi₂O₃/TiO₂ composites

was added to the calculated amount of the above graphene solution to prepare 0.5, 1 and 3 wt% graphene coupled 3 mol% Bi₂O₃/TiO₂ (T3) composites with the different amounts of graphene in the composites. The samples with different mass ratios of graphene to T3 samples (0, 0.5, 1 and 3 wt%) were labeled as T3, T3G0.5, T3G1 and T3G3, respectively. The mixing solution was aged under vigorous stirring for 2 h to obtain a homogeneous suspension. Then, this suspension was transferred to a 30 mL Teflon-sealed autoclave and maintained at 120 °C for 24 h. After the hydrothermal treatment, the resulting composites were recovered by filtration, washed with water, and then fully dried at 60 °C in an oven to obtain the Bi₂O₃/TiO₂/graphene composites with varying amounts of graphene.

2.3. Characterization

The samples were characterized with X-ray diffraction (XRD) with Cu K_α radiation ($\lambda = 1.54178 \text{ \AA}$). The morphology of samples were studied by field emission scanning electron microscopy (FESEM, JEOL 6340F) with energy-dispersive spectra (EDS) and transmission electron microscopy (TEM, Philips CM30). The high resolution TEM image was acquired using a JEOL 4000EX microscopy, operated at 400 kV. The chemical states of the samples were determined by X-ray photoelectron spectroscopy (XPS) in a VG Multilab 2009 system (UK) with a monochromatic Al K_α source and charge neutralizer. The surface states of the photocatalysts before and after degradation reaction. The surface area of the samples were measured by TriStar 3000-BET/BJH Surface Area. The UV–vis absorbance spectra were obtained for the samples using a scan UV–vis spectrometer (Shimadzu UV-2550, Japan). Photoluminescence (PL) spectra were measured at room temperature using a fluorescence spectrophotometer (PerkinElmer LS55) with an excitation wavelength of 380 nm.

2.4. Photocatalytic test

Photocatalysis reactions were performed in an air-free, closed gas circulation system with a quartz reaction cell. Photocatalytic activity was evaluated by the degradation of Rhodamine B (RhB) in aqueous solution under visible-light irradiation using a 300 W Xe lamp with a cutoff filter ($\lambda > 420 \text{ nm}$). A cylindrical Pyrex flask (200 mL) was placed in a sealed black box of which the top was open and the cutoff filter was set on the window face of the reaction vessel to ensure the desired irradiation condition. In each experiments, the samples as catalysts (0.2 g) were added into RhB solution ($1 \times 10^{-5} \text{ M}$, 100 mL). Before illumination, the suspension between photocatalyst powders and RhB at given time intervals (3 mL aliquots) were sampled and centrifuged to remove photocatalyst powders. The filtrates were analyzed by recording the variations of the absorption-band maximum (554 nm) in the UV–vis spectrum of RhB in aqueous solution using a UV–vis spectrophotometer (Shimadzu 2550, Japan).

3. Results and discussion

3.1. Characterization of Bi₂O₃/TiO₂ nanocomposites

The phase composition and crystallinity of the as-prepared Bi₂O₃ modified TiO₂ samples were characterized by XRD, as shown in Fig. 1. Predominantly characteristic peaks can be indexed according to TiO₂ crystalline phase (JCPDS, Card No. 8621-1272), which is in agreement with the previous works [22]. It illustrates that doping with Bi₂O₃ does not result in the development of new crystal orientations or changes in preferential orientations, implying the small size and extremely high dispersion of Bi₂O₃ species [30]. These peaks in the patterns were indexed to (101), (004), (200),

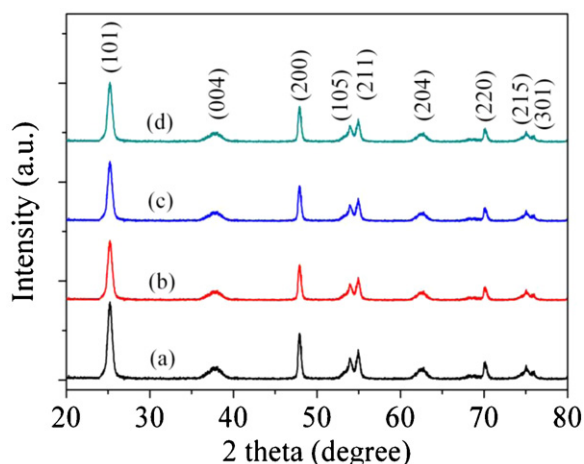


Fig. 1. The XRD patterns of the as-prepared $\text{Bi}_2\text{O}_3/\text{TiO}_2$ composites with various content of Bi_2O_3 (a) T0, (b) T1, (c) T3, (d).

(105), (211), (204), (220), (215) and (301) planes respectively, which indicates that all samples are constituted of anatase TiO_2 phase [22]. However, the crystallization degree decreased a little with the increase of the content of Bi_2O_3 species up to 1 mol% and then remained almost unchanged with the further increase of the content of Bi_2O_3 species from 1 to 5 mol%.

TEM images show that the as-prepared products consist of well-defined sheet-shaped structures having a rectangular outline, with an average side size of about 50 nm, as shown in Fig. 2a. The high-resolution TEM image shown in Fig. 2b, directly presents that the lattice spacing parallel to the top and bottom facets is ca. 0.235 nm, corresponding to the (001) planes of the crystallized anatase TiO_2 . Especially, the HRTEM image also showed clearly that a large number of nanoparticles with average diameter around 2 nm was homogeneously dispersed on the surface of TiO_2 nanosheets with exposed {001} facets (also see Fig. S1, Supporting information), which indicated a nanocrystal heterojunction to be formed in the composites.

In order to index the phase of quantum dots on TiO_2 nanosheets, quantitative XPS analysis is performed on T3 samples. Fig. 3 shows the typical full survey and high-resolution spectra for the Ti 2p and Bi 4f region. Fig. 3a shows T0 sample contains only Ti, O and C elements while T3 sample contains Ti, O, Bi and C elements. The C element can be ascribed to the adventitious hydrocarbon from the XPS instrument itself. Furthermore, the binding energies of Ti 2p_{3/2} and Ti 2p_{1/2} are equal to 458.9 and 464.4 eV, respectively (see Fig. 3c), which showed the main valence of Ti in the prepared catalysts is +4 and Ti^{4+} is in tetrahedral coordination with oxygen. Besides, high-resolution XPS spectrum of Bi 4f region is shown in Fig. 3d. The peaks centered at 164.2 eV and 158.9 eV, showing the +3 valence state of Bi cation, which could be designed to Bi_2O_3 [24]. These results suggested that the Bi_2O_3 and TiO_2 were present mainly as separate phases in $\text{Bi}_2\text{O}_3/\text{TiO}_2$ composites, respectively.

The UV–vis absorption spectra for various samples are discussed. The hybridization of Bi_2O_3 quantum dots with TiO_2 nanosheets in the composites for the T0–T5 samples has resulted in absorption edge varying to nearly 420 nm within the visible light region. Furthermore, the UV–vis absorption spectra for the $\text{Bi}_2\text{O}_3/\text{TiO}_2$ composites with increasing Bi_2O_3 content (1–5 mol%), were shown in Fig. 4. Light absorbance of the $\text{Bi}_2\text{O}_3/\text{TiO}_2$ sample in the visible light region is of great importance for its photocatalytic application since it could be even activated by sunlight.

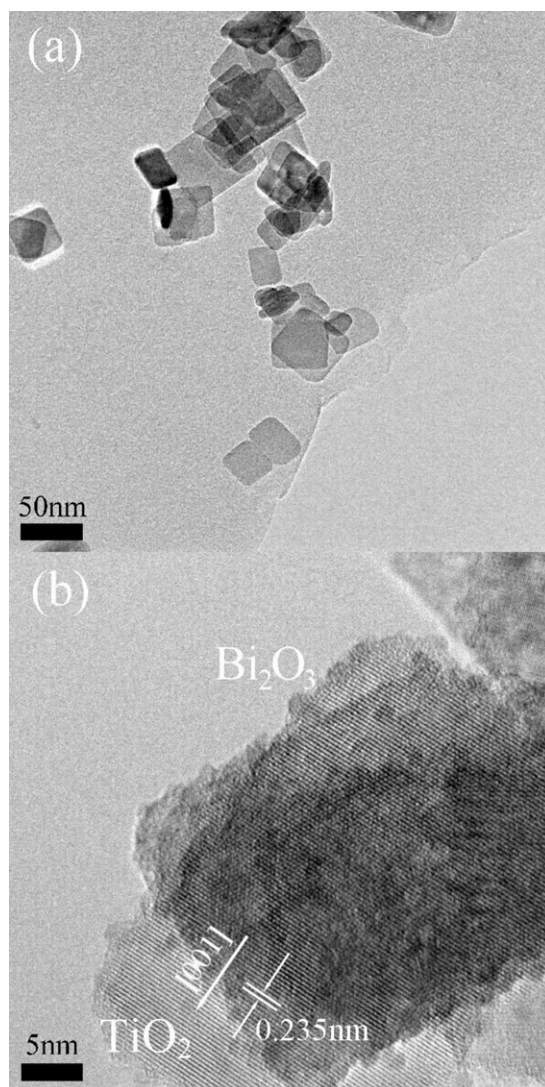


Fig. 2. The TEM and HRTEM images of the $\text{Bi}_2\text{O}_3/\text{TiO}_2$ composites (T3 sample).

3.2. Photocatalytic degradation of $\text{Bi}_2\text{O}_3/\text{TiO}_2$ composites

The photocatalytic activities of the samples were evaluated by monitoring the decomposition of RhB in an aqueous solution under visible light irradiation, respectively. RhB solution is also a common model pollutant to test the photodegradation capability of the $\text{Bi}_2\text{O}_3/\text{TiO}_2$ samples. Table 1 summarizes the catalytic activities of the $\text{Bi}_2\text{O}_3/\text{TiO}_2$ samples measured in photocatalytic degradation of RhB under visible irradiation. Although the pure TiO_2 could not be activated by visible lights, it still displayed 67% degradation yield of RhB dye within 60 min, possibly owing to the formation of surface complex between RhB dye and TiO_2 , which might absorb visible light and induce the degradation of RhB dye [22]. As shown in Fig. 5, it is interesting that, with the increase of Bi_2O_3 content from

Table 1
Effect of Bi_2O_3 content on degradation efficiency for $\text{Bi}_2\text{O}_3/\text{TiO}_2$ samples.

Samples	Contents of Bi_2O_3	Degradation efficiency (60 min)	Reaction kinetic rate
T0	0 mol%	67%	0.01698
T1	1 mol%	77%	0.02532
T3	3 mol%	99%	0.05315
T5	5 mol%	90%	0.03773

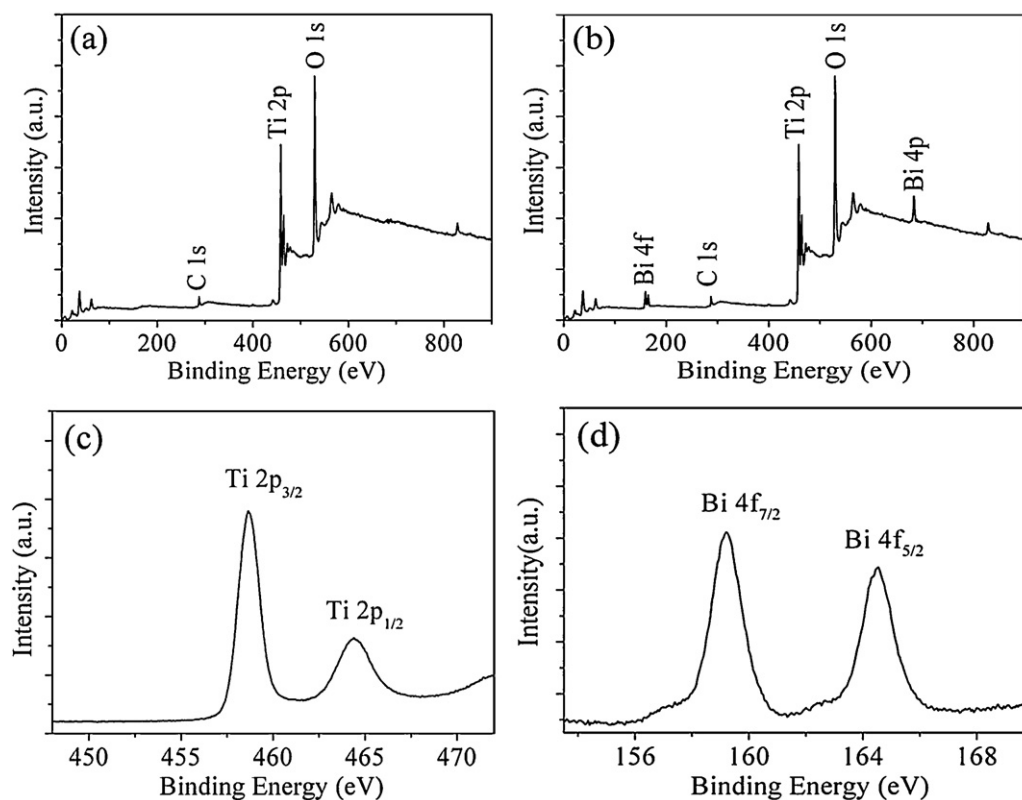


Fig. 3. The XPS spectra: survey spectrum of (a) TiO_2 nanosheets and (b) 3 mol% Bi_2O_3 decorated TiO_2 nanosheets, (c) Ti 2p, (d) Bi 4f.

1 to 3%, the activity of the $\text{Bi}_2\text{O}_3/\text{TiO}_2$ increased gradually owing to the enhanced absorbance for visible lights and the increase of surface area, which facilitated the adsorption for RhB molecules. However further increase of the Bi/Ti molar ratio to 5% caused a slight decrease in the activity, which could be mainly attributed to the decreased surface area, taking into account of the similar light absorbance. For the $\text{Bi}_2\text{O}_3/\text{TiO}_2$ system (Fig. 6), however, the absorption bands of RhB show two types of spectral changes. One is a hypsochromic shift in the absorbance maximum; the other is a decrease in absorbance. The absorbance maximum of RhB shifts gradually from 554 to 510 nm; concurrently, the absorption peaks of the dye remarkably fade away. Moreover, absorption peaks located at wavelengths lower than 400 nm also decrease rapidly during the illumination period. The product after 60 min of illumination, which has an absorption peak at 510 nm, can be identified as an incompletely N-deethylated outcome of RhB, N-ethyl

rhodamine [31]. The final degradation efficiency of the 3 mol% Bi_2O_3 quantum dots decorated TiO_2 nanosheets demonstrate that the highest photocatalytic efficiency (ca. 99%) was obtained among these specimens.

On one side, the higher activity of the $\text{Bi}_2\text{O}_3/\text{TiO}_2$ could be attributed to the larger surface area that facilitated the diffusion RhB molecules and thus, promoted the adsorption on the photocatalyst. And the relative surface area for $\text{Bi}_2\text{O}_3/\text{TiO}_2$ sample will show in the part of $\text{Bi}_2\text{O}_3/\text{TiO}_2$ /graphene composites. On the other side, the $\text{Bi}_2\text{O}_3/\text{TiO}_2$ contained smaller Bi_2O_3 quantum dots which might enhance the photosensitizing effect from Bi_2O_3 , leading to the higher absorbance for visible lights. More importantly, the $\text{Bi}_2\text{O}_3/\text{TiO}_2$ displayed stronger interaction between Bi_2O_3 and TiO_2 , which could further enhance the Bi_2O_3 photosensitization and also inhibit the recombination between photo-induced electrons and holes.

Generally, the decomposition of the dye could be assigned to a pseudo-first-order kinetics reaction with a simplified Langmuir–Hinshelwood model when C_0 is very small.

$$\ln\left(\frac{C_0}{C}\right) = kt$$

where k is the apparent first-order kinetics rate constant, and was determined from a linear fit to the data as shown in Fig. 6. Clearly, T3 sample gave a rate constant of dye degradation 3 times higher than pure TiO_2 nanosheets. In addition, the photodegradation of RhB that was monitored over four cycles each of 60 min (as shown in Fig. S2, Supporting information). After each cycle, the photocatalytic efficiency exhibited only a slight decrease and no significant loss of activity after the decomposition was repeated four consecutive times, indicating that T3 composite was an efficient and stable visible-light photocatalyst.

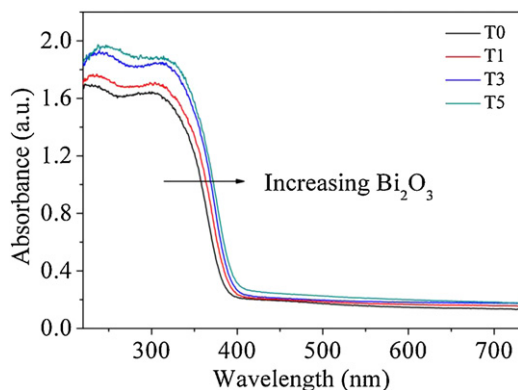


Fig. 4. The UV-vis spectra of the $\text{Bi}_2\text{O}_3/\text{TiO}_2$ composites using different amounts of Bi_2O_3 .

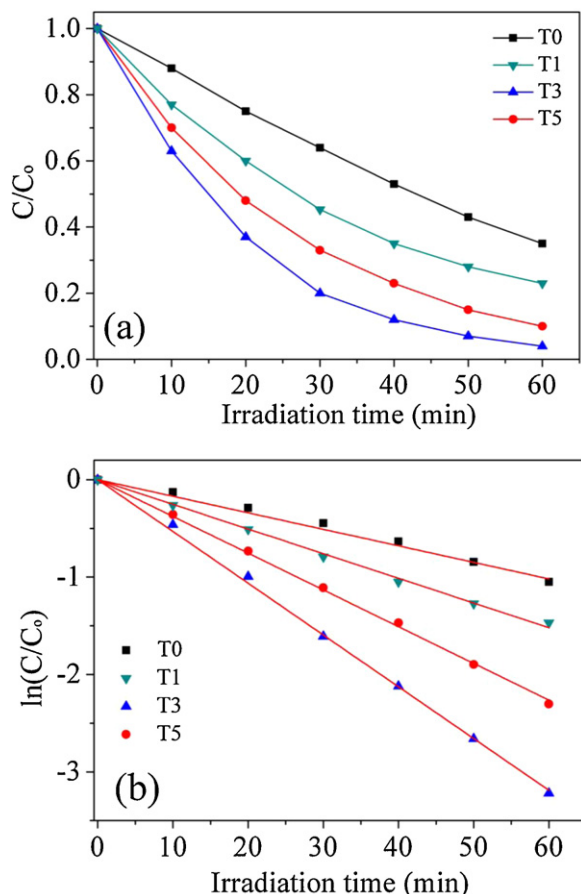


Fig. 5. Evaluation of photocatalytic activities (a) and the relative kinetic rates (b) in RhB degradation with TiO_2 nanosheets decorated with different content of Bi_2O_3 under visible-light irradiation.

3.3. Graphene decorated $\text{Bi}_2\text{O}_3/\text{TiO}_2$ nanocomposites

Currently, the utilization of graphene is an active area of research. In this work, the graphene sheets decorated $\text{Bi}_2\text{O}_3/\text{TiO}_2$ composites (graphene- $\text{Bi}_2\text{O}_3/\text{TiO}_2$) were facilely prepared via a hydrothermal process in an ethanol–water solvent. The crystal structure of graphene- $\text{Bi}_2\text{O}_3/\text{TiO}_2$ composites from the XRD patterns were showed (see Fig. S3, Supporting information). It is evident that no characteristic diffraction peaks for carbon species are observed in the patterns because of the low amount and relatively low diffraction intensity of graphene. In addition, there is nearly no change in the crystal structure of TiO_2 after the hybridization with Bi_2O_3 quantum dots and graphene sheets.

Moreover, the morphologies of graphene- $\text{Bi}_2\text{O}_3/\text{TiO}_2$ composites along with the bare graphene for comparison were characterized by TEM and HRTEM, as shown in Fig. 7. It can be seen that the $\text{Bi}_2\text{O}_3/\text{TiO}_2$ composites are distinctly coupled with graphene sheets as shown in Fig. 7a. The two-dimensional structure of graphene sheets with micrometers-long wrinkles is still retained after the hydrothermal treatment of graphene and $\text{Bi}_2\text{O}_3/\text{TiO}_2$ composites, which is similar to reports from previous work [27]. In addition, it is difference among graphene/ $\text{Bi}_2\text{O}_3/\text{TiO}_2$ composites (as shown in Fig. 7b) compared with pure TiO_2 nanosheets (as shown in Fig. 2a), demonstrating that plenty of nanoparticles were mixed with graphene and TiO_2 sheets. Fig. 7c and d shows the HRTEM images also showed clearly that a large number of quantum dots with average diameter around 2 nm were homogeneously dispersed on the surface of TiO_2 sheets coupled with graphene, which also indicated the graphene- $\text{Bi}_2\text{O}_3/\text{TiO}_2$ composites were formed.

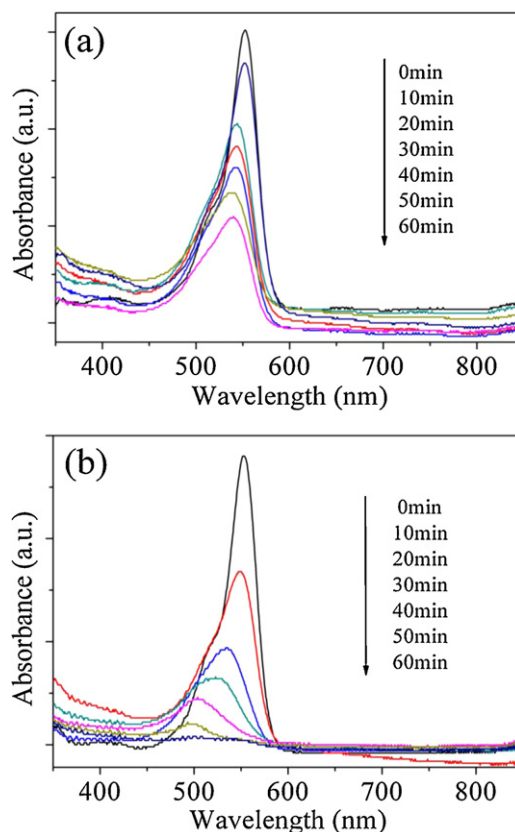


Fig. 6. UV–visible spectra changes in RhB degradation with TiO_2 nanosheets (a) and Bi_2O_3 quantum dots decorated TiO_2 nanosheets (b) under visible-light irradiation.

Besides, the energy-dispersive spectra (EDS) analysis data of 3 mol% $\text{Bi}_2\text{O}_3/\text{TiO}_2$ sample were conducted and the molar ratio of bismuth to titanium was about 0.06, confirming that the white circles in Fig. 7 have been proved the Bi_2O_3 quantum dots.

Quantitative XPS analysis is performed on T3G1 samples. Fig. 8 shows the typical full survey and high-resolution spectra for the Ti 2p, C 1s and Bi 4f region. As shown in Fig. 8a, graphene contains only O and C elements while T3G1 sample contains Ti, O, Bi and C elements (see Fig. 8b), demonstrating that the incorporation of $\text{Bi}_2\text{O}_3/\text{TiO}_2$ composites contributed to the intensity of O and C element, but the C/O ratio in the graphene was still increased remarkably. In the previous works, the peak centered at 284.5 eV is attributed to nonoxygenated C–C linkages, which could be designed to graphene [32,33]. As shown in Fig. 8c, while the peaks at the binding energy ranges of 286.0–286.5 eV, 287.4–287.7 eV, and 288.4–288.8 eV were attributed to the C–OH, C=O, and O=C–OH oxygen-containing carbonaceous bands, respectively [32,33]. There is an appreciable drop in the peak intensity after irradiation in the presence of the photocatalyst. This clearly illustrates that photocatalytic deoxygenation are effectively being carried out during the course of the irradiation, which is consistent with the previous reports [27]. These results suggested that the graphene, Bi_2O_3 and TiO_2 were present mainly as separate phases in graphene- $\text{Bi}_2\text{O}_3/\text{TiO}_2$ composites, respectively.

Further investigation was carried out by full nitrogen sorption isotherms to gain the information about the specific surface area, as shown in Fig. 9, nitrogen adsorption–desorption measurements along with the Brunauer–Emmet–Teller (BET) and Barrett–Joyner–Halenda (BJH) methods were used. The isotherm could be classified as a type-IV isotherm with a H1 hysteresis loop, which was characteristic of the mesoporous material present within the graphene- $\text{Bi}_2\text{O}_3/\text{TiO}_2$ composites. As shown in Fig. 9,

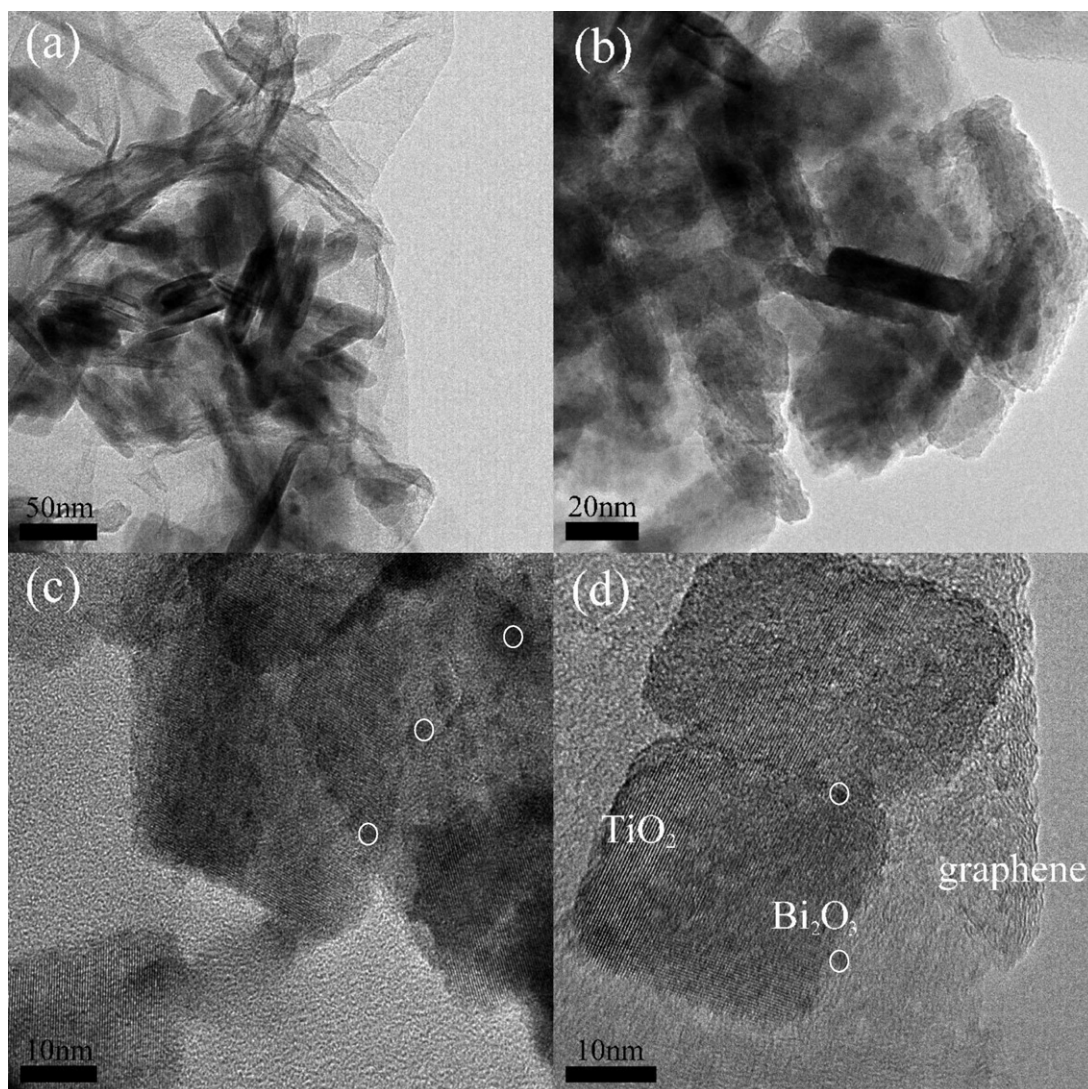


Fig. 7. The TEM and HRTEM images of the as-prepared 1 wt% graphene-Bi₂O₃/TiO₂ (T3G1 sample).

the specific surface area of the graphene-Bi₂O₃/TiO₂ composites was calculated to be 164 m² g⁻¹ based on the BET analysis, which was slightly higher than that of Bi₂O₃/TiO₂ nanosheets (78 m² g⁻¹) and P25 (50 m² g⁻¹). The corresponding BJH analyses for the graphene-Bi₂O₃/TiO₂ composites exhibit that most of the pores fall into the size range from 3 to 33 nm, as shown in Fig. 9. It was supposed that tiny holes and narrow gaps existing between the individual graphene/Bi₂O₃/TiO₂ composites were playing a role as pores. The high surface area and mesoporous structure of the graphene-Bi₂O₃/TiO₂ composites provide the possibility for the efficient diffusion and transportation of the degradable organic molecules and hydroxyl radicals in photochemical reaction, which will lead to the enhanced photocatalytic performance of the graphene-Bi₂O₃/TiO₂ materials.

The UV-vis absorption spectra for 1 wt% graphene coupled Bi₂O₃/TiO₂ composites were shown in Fig. 10. With increase in the graphene oxide content, an enhanced absorption in the visible light region is obtained, which is similar to the previous reports [32,33]. Meanwhile, a red shift to higher wavelength in the absorption edge of P25-graphene nanocomposites has also been observed using the P25-1% graphene nanocomposite for liquid-phase degradation of methylene blue in the previous works [27,34], therefore indicating a narrowing of the band gap of P25. Besides, the presence of graphene leads to a continuous absorption band in the range

of 400–800 nm and the strong absorption intensity, which is in agreement with the black color of the samples and high photocatalytic activity for a given reaction [27,34]. Because of the increased absorbance, a more efficient utilization of the solar energy can be obtained. Thus, the hybridization of graphene in Bi₂O₃/TiO₂ composite is effective for the visible-light response of the composite.

3.4. Photocatalytic degradation of Bi₂O₃/TiO₂/graphene composites

Table 2 summarizes the catalytic activities of the graphene-Bi₂O₃/TiO₂ samples for the degradation of RhB under visible irradiation. Although the T3 sample displayed 95%

Table 2
Effect of graphene content on degradation efficiency for graphene-Bi₂O₃/TiO₂ samples.

Samples	Contents of graphene	Degradation efficiency (50 min)	Reaction kinetic rate
T3	0	95%	0.05315
T3G0.5	0.5 wt%	97%	0.06308
T3G1	1 wt%	99.7%	0.08883
T3G3	3 wt%	88%	0.04182

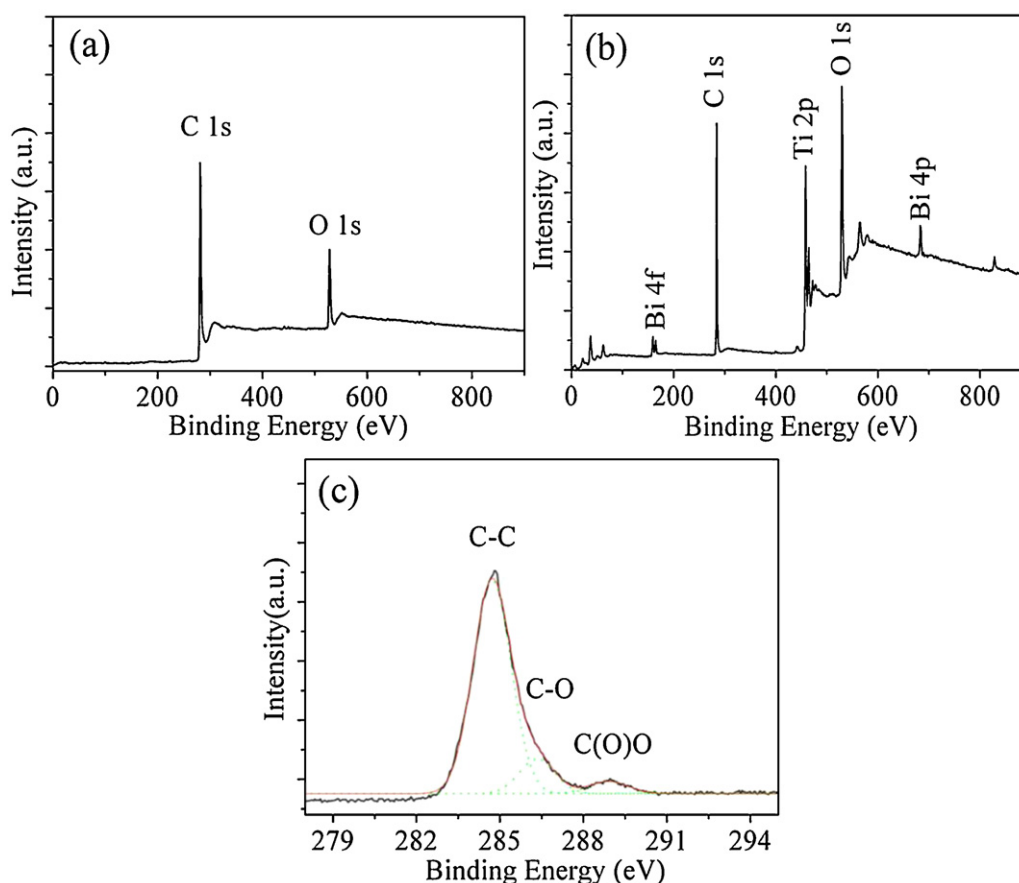


Fig. 8. The XPS spectra: survey spectrum of (a) graphene and (b) 1 wt% graphene coupled $\text{Bi}_2\text{O}_3/\text{TiO}_2$ composites (T3G1 sample), (c) C 1s.

degradation yield of RhB dye within 50 min, it is interesting that, with the increase of graphene content from 0.5 to 3%, the activity of the $\text{Bi}_2\text{O}_3/\text{TiO}_2$ increased gradually owing to the enhanced absorbance for visible lights and the increase of surface area, which facilitated the adsorption for RhB molecules, as shown in Fig. 11. However further increase of the graphene and $\text{Bi}_2\text{O}_3/\text{TiO}_2$ mass ratio to 3% caused a slight decrease in the activity. Obviously, T3G1 gave a rate constant of dye degradation 1.7 times higher than T3 samples. As comparison, the blank experiment about the photocatalytic activity of TiO_2 nanosheets and anatase TiO_2 nanocrystals with exposed {001} facets on graphene sheets has been shown (see Fig. S4, Supporting information), confirming the advantage of

$\text{Bi}_2\text{O}_3/\text{TiO}_2/\text{graphene}$. Currently, to evaluate the adsorption ability of TiO_2 nanosheets, $\text{Bi}_2\text{O}_3/\text{TiO}_2$ and $\text{Bi}_2\text{O}_3/\text{TiO}_2/\text{graphene}$ composites catalysts, the degradation of RhB was performed in the dark, as presented in Fig. S5. $\text{Bi}_2\text{O}_3/\text{TiO}_2/\text{graphene}$ composites adsorbed more RhB than TiO_2 nanosheets, which could be attributed to the large surface area of the composites catalysts.

In addition, it is worth pointing out that the stability of a given photocatalyst during photoreaction is a crucial factor for the practical applications. The photodegradation of RhB that was monitored over four cycles each of 50 min (see Fig. S6, Supporting information). After each cycle, the photocatalytic efficiency exhibited only a slight decrease and no significant loss of activity after the fourth times decomposition. Compared with the XRD patterns

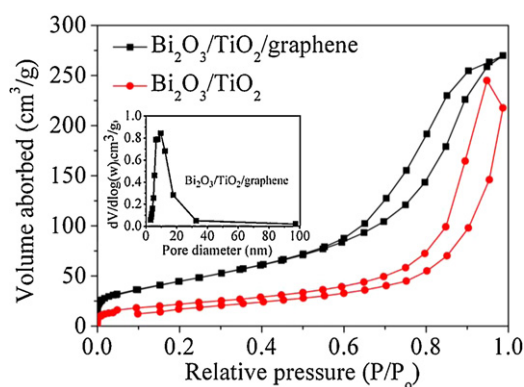


Fig. 9. Typical N_2 gas adsorption–desorption isotherms and the corresponding pore-size distribution of 3 mol% Bi_2O_3 quantum dots decorated TiO_2 nanosheets and 3 mol% Bi_2O_3 quantum dots decorated TiO_2 nanosheets coupled with graphene.

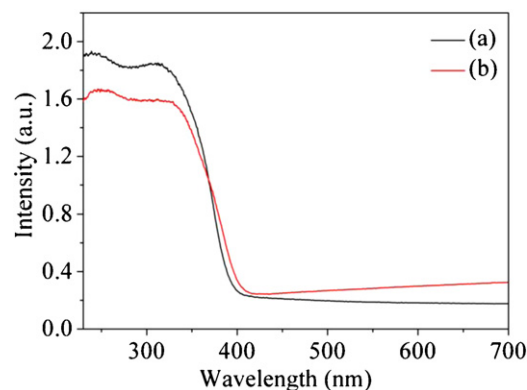


Fig. 10. The UV–vis spectra of the $\text{Bi}_2\text{O}_3/\text{TiO}_2$ composites using different contents of graphene.

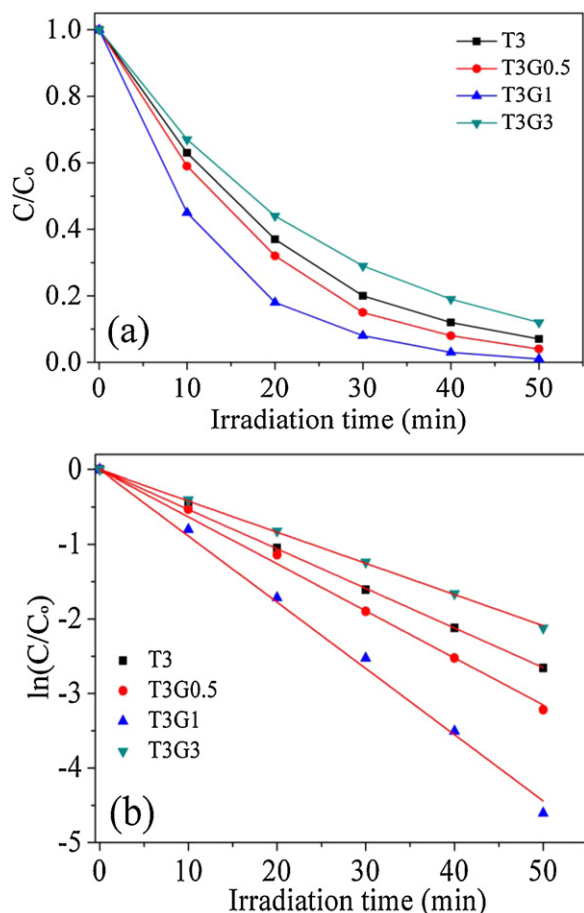


Fig. 11. Evaluation of photocatalytic activities (a) and kinetic rates (b) in RhB degradation with $\text{Bi}_2\text{O}_3/\text{TiO}_2$ composites coupled with different content of graphene under visible-light irradiation.

of $\text{Bi}_2\text{O}_3/\text{TiO}_2/\text{graphene}$ composites before and after photocatalysis (see Fig. S7, Supporting information), no second phase was observed after the final degradation. Thus, all results indicate that T3G1 nanocomposite is also an efficient and stable visible-light photocatalyst.

3.5. Tentative photocatalytic mechanism

It is interesting to explore the tentative mechanism for this significant enhanced photocatalytic performance, as schematically demonstrated in Fig. 12. The positions of the valence band maximum (V_{BM}) and the conduction band minimum (C_{BM}) are critical variables in determining the feasibility of photocatalytic activity. According to the following empirical equation [35,36], where E_{VB} is the VB edge potential, X is the electronegativity of the semiconductor, which is the geometric mean of the electronegativity of the constituent atoms, E° is the energy of free electrons on the hydrogen scale (~ 4.5 eV), E_g is the band gap energy of the semiconductor, and E_{CB} can be determined by $E_{\text{CB}} = E_{\text{VB}} - E_g$. The X value for Bi_2O_3 is ca. 5.986 eV. The conduction band (CB) and valence band (VB) potentials of Bi_2O_3 are 0.11 eV and 2.86 eV, respectively.

$$E_{\text{CB}} = X - E^\circ - 0.5E_g$$

In the previous report about TiO_2 for hydrogen production from water splitting [37], it is concluded that the CB edge potential of TiO_2 is higher than the H^+/H_2 reduction potential. Thus, the CB edge potential of TiO_2 is more active than that of Bi_2O_3 (0.11 eV); hence, photoinduced electrons on the TiO_2 nanosheet surface

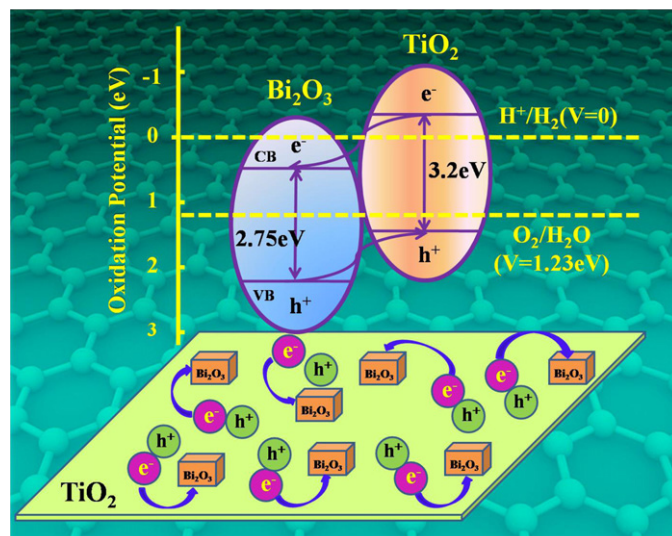


Fig. 12. Schematic illustration of the charge separation and transfer in the $\text{graphene-Bi}_2\text{O}_3/\text{TiO}_2$ system under visible-light. The photoexcited electrons transfer from the conduction band of semiconductor $\text{Bi}_2\text{O}_3/\text{TiO}_2$ composite.

transfer easily to Bi_2O_3 via interfaces; similarly, photoinduced holes on the Bi_2O_3 surface migrate to TiO_2 nanosheet owing to the different VB edge potentials, as shown in Fig. 12. Therefore, a larger amount of electrons on the Bi_2O_3 surface and holes on the TiO_2 surface, respectively, can participate in photocatalytic reactions to directly or indirectly decompose RhB, resulting in the enhanced photocatalytic activity.

In addition, the $\text{Bi}_2\text{O}_3/\text{TiO}_2$ composites contained a large number of Bi_2O_3 quantum dots might enhance the photosensitizing effect from Bi_2O_3 , leading to the higher absorbance for visible lights. Especially, the Bi_2O_3 quantum dots decorated TiO_2 nanosheets exhibited stronger interaction between Bi_2O_3 quantum dots and TiO_2 nanosheets, which could further improve the Bi_2O_3 quantum dots photosensitization and also inhibit the recombination between photogenerated electrons and holes. Obviously, the tightly chemical bonding between Bi_2O_3 quantum dots and TiO_2 nanosheets, plays a pivot role in stabilizing Bi_2O_3 species against leaching, resulting into the longer lifetime. Furthermore, it is proposed that this chemical bonding may be ascribed to the polar interaction which expected to be more favorable for promoting interface charge carrier transfer in the heterostructures [38,39].

Furthermore, graphene has high charge carrier mobility, and thus the electron is now mobilized on the graphene sheet. The presence of graphene suspended in solution reduces the possible recombination of charge carriers, which in turn results in enhanced photocatalytic performance in $\text{graphene-Bi}_2\text{O}_3/\text{TiO}_2$ composites. One issue with graphene is that it does absorb a certain amount of light, and thus at higher content of graphene in the composites there is a competition for light absorption. This may explain the decreasing efficiency at 3 wt% graphene. On the other side, the separation of photogenerated electron-hole pairs is also accelerated by {001} facets. In general, the interfacial electron transfer is mediated by the surface defects. Typically, high-energy {001} facets are composed of high densities of undercoordinated Ti atoms and a very large Ti–O–Ti bond angle, forming abundant oxygen deficiency [28].

For semiconductors, the photoluminescence (PL) spectra are related to the transfer behavior of the photoinduced electrons and holes, so that it can reflect the separation and recombination of photoinduced charge carriers [33]. The PL spectra of the as-prepared TiO_2 , $\text{Bi}_2\text{O}_3/\text{TiO}_2$ composites and $\text{graphene-Bi}_2\text{O}_3/\text{TiO}_2$ composites are shown in Fig. 13. The excitation wavelength is determined as

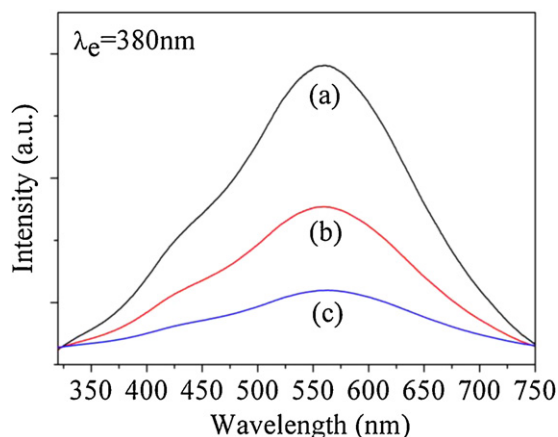


Fig. 13. Photoluminescence spectra of TiO_2 , $\text{Bi}_2\text{O}_3/\text{TiO}_2$ composites and graphene- $\text{Bi}_2\text{O}_3/\text{TiO}_2$ composites excited at the wavelength of 380 nm.

380 nm, and the TiO_2 nanosheet has a strong emission peak at about 560 nm. The PL intensities of $\text{Bi}_2\text{O}_3/\text{TiO}_2$ composites decreased with an addition of Bi_2O_3 quantum dots. Furthermore, there was a small PL peak observed for graphene- $\text{Bi}_2\text{O}_3/\text{TiO}_2$ composites, indicating that the electron–hole pairs recombination is very slow. This is ascribed to the fact that graphene- $\text{Bi}_2\text{O}_3/\text{TiO}_2$ composites could prevent the direct recombination of electrons and holes.

Acknowledgments

This work was supported by National Science Foundation of China (no. 51102015, 51004008 and 21071014), the Fundamental Research Funds for the Central Universities (no. FRF-AS-11-002A and FRF-TP-12-023A), China Postdoctoral Science Foundation (no. 20110490009), Research Fund for the Doctoral Program of Higher Education of China (no. 20110006120027), and the Program for New Century Excellent Talents in University (NCET-11-0577).

Appendix A. Supplementary data

Supplementary data associated with this article can be found, in the online version, at <http://dx.doi.org/10.1016/j.apcatb.2012.09.009>.

References

- [1] Y. Yin, A.P. Alivisatos, *Nature* 437 (2005) 664.
- [2] N. Tian, Z.Y. Zhou, S.G. Sun, Y. Ding, Z.L. Wang, *Science* 316 (2007) 732.
- [3] X. Chen, S. Mao, *Chem. Rev.* 107 (2007) 2891.
- [4] H.G. Yang, C.H. Sun, S.Z. Qiao, J. Zou, G. Liu, S.C. Smith, H.M. Cheng, G.Q. Lu, *Nature* 453 (2008) 638.
- [5] X. Han, M. Jin, S. Xie, Q. Kuang, Z. Jiang, Y. Jiang, Z. Xie, L. Zheng, *Angew. Chem. Int. Ed.* 121 (2009) 9344.
- [6] M. Lazzeri, A. Vittadini, A. Selloni, *Phys. Rev. B* 63 (2001) 155409.
- [7] A. Vittadini, A. Selloni, F.P. Rotzinger, M. Grätzel, *Phys. Rev. Lett.* 81 (1998) 2954.
- [8] U. Diebold, *Surf. Sci. Rep.* 48 (2003) 53.
- [9] J. Zhang, M.R. Langille, M.L. Personick, K. Zhang, S. Li, C.A. Mirkin, *J. Am. Chem. Soc.* 132 (2010) 14012.
- [10] X.Q. Gong, A. Selloni, *J. Phys. Chem. B* 109 (2005) 19560.
- [11] A. Hameed, T. Montini, V. Gombac, P. Fornasiero, *J. Am. Chem. Soc.* 130 (2008) 9658.
- [12] J. Zhang, Q. Xu, Z.C. Feng, M.J. Li, C. Li, *Angew. Chem. Int. Ed.* 47 (2008) 1766.
- [13] X.H. Yang, Z. Li, C.H. Sun, H.G. Yang, C.Z. Li, *Chem. Mater.* 23 (2011) 3486.
- [14] S.W. Liu, J.G. Yu, M. Jaroniec, *Chem. Mater.* 23 (2011) 4085.
- [15] A.S. Barnard, L.A. Curtiss, *Nano Lett.* 5 (2005) 1261.
- [16] H.G. Yang, H.C. Zeng, *J. Am. Chem. Soc.* 127 (2005) 270.
- [17] H.G. Yang, H.C. Zeng, *J. Phys. Chem. B* 108 (2004) 3492.
- [18] G. Liu, H.G. Yang, X.W. Wang, L.N. Cheng, J. Pan, G.Q. Lu, H.M. Cheng, *J. Am. Chem. Soc.* 131 (2009) 12868.
- [19] Q.J. Xiang, J.G. Yu, W.G. Wang, M. Jaroniec, *Chem. Commun.* 47 (2011) 6906.
- [20] G. Liu, C.H. Sun, S.C. Smith, L.Z. Wang, G.Q. Lu, H.M. Cheng, *J. Colloid Interface Sci.* 349 (2010) 477.
- [21] J.G. Yu, G.P. Dai, Q.J. Xiang, M. Jaroniec, *J. Mater. Chem.* 21 (2011) 1049.
- [22] J. Zhu, S.H. Wang, J.G. Wang, D.Q. Zhang, H.X. Li, *Appl. Catal., B* 102 (2011) 120.
- [23] L.F. Qi, J.G. Yu, M. Jaroniec, *Phys. Chem. Chem. Phys.* 13 (2011) 8915.
- [24] J.G. Hou, Z. Wang, S.Q. Jiao, H.M. Zhu, J. Hazard. Mater. 192 (2011) 1772.
- [25] A.K. Geim, K.S. Novoselov, *Nat. Mater.* 6 (2007) 183.
- [26] A.K. Geim, *Science* 324 (2009) 1530.
- [27] Y.H. Zhang, Z.R. Tang, X.Z. Fu, Y.J. Xu, *ACS Nano* 4 (2010) 7303.
- [28] L. Sun, Z.L. Zhao, Y.C. Zhou, L. Liu, *Nanoscale* 4 (2012) 613.
- [29] W.S. Hummers, R.E. Offeman, *J. Am. Chem. Soc.* 80 (1958) 1339.
- [30] Z.F. Bian, J. Zhu, S.H. Wang, Y. Cao, X.F. Qian, H.X. Li, *J. Phys. Chem. C* 112 (2008) 6258.
- [31] J.D. Zhuang, W.X. Dai, Q.F. Tian, Z.H. Li, L.Y. Xie, J.X. Wang, P. Liu, *Langmuir* 26 (2010) 9686.
- [32] Q. Li, B.D. Guo, J.G. Yu, J.R. Ran, B.H. Zhang, H.J. Yan, J.R. Gong, *J. Am. Chem. Soc.* 133 (2011) 10878.
- [33] J.G. Hou, Z. Wang, W.B. Kan, S.Q. Jiao, H.M. Zhu, *J. Mater. Chem.* 22 (2012) 7291.
- [34] H. Zhang, X.J. Lv, Y.M. Li, Y. Wang, J.H. Li, *ACS Nano* 4 (2010) 380.
- [35] M.A. Butler, D.S. Ginley, *J. Electrochem. Soc.* 125 (1978) 228.
- [36] X.P. Lin, J.C. Xing, W.D. Wang, Z.C. Shan, F.F. Xu, F.Q. Huang, *J. Phys. Chem. C* 111 (2007) 18288.
- [37] A. Fujishima, K. Honda, *Nature* 238 (1972) 37.
- [38] X.W. Wang, L.C. Yin, L. Gang, L.Z. Wang, R. Saito, G.Q. Lu, H.M. Cheng, *Energy Environ. Sci.* 4 (2011) 3976.
- [39] J.G. Hou, Z. Wang, S.Q. Jiao, H.M. Zhu, *CrystEngComm* 14 (2012) 5923.